Universality in quasiperiodic Rayleigh-Bénard convection

R. E. Ecke, Ronnie Mainieri, and T. S. Sullivan
Physics Division and Center for Nonlinear Studies, Los Alamos National Laboratory, Los Alamos, New Mexico 87545
(Received 1 April 1991)

We study universal scaling properties of quasiperiodic Rayleigh-Bénard convection in a ^{3}He–superfluid-^{4}He mixture. The critical line is located in a parameter space of Rayleigh and Prandtl numbers using a transient-Poincaré-section technique to identify transitions from nodal periodic points to spiral periodic points within resonance horns. We measure the radial and angular contraction rates and extract the linear-stability eigenvalues (Flouquet multipliers) of the periodic point. At the crossings of the critical line with the lines of fixed golden-mean-tail winding number we determine the universality class of our experimental dynamics using $f(\alpha)$ and trajectory-scaling-function analyses. A technique is used to obtain a robust five-scale approximation to the universal trajectory scaling function. Different methods of multifractal analysis are employed and an understanding of statistical and systematic errors in these procedures is developed. The power law of the inflection point of the map, determined for three golden-mean-tail winding numbers, is 2.9 ± 0.3, corresponding to the universality class of the sine-circle map.

PACS number(s): 47.25.−c, 05.45.+b, 67.60.Fp

I. INTRODUCTION

One of the most studied transitions to chaos in dynamical systems is the transition from a quasiperiodic (two incommensurate frequencies) state [1–3]. This state can be an intrinsic two-frequency state where internal oscillatory modes, characterized by different frequencies, interact, or it can be a single oscillatory mode that is forced by an external oscillator of variable frequency and amplitude. Although the two-internal-mode system is fundamentally more complicated because there is an additional degree of freedom relative to the forced system, the two share many common features. The state of either system is often completely characterized by the ratio of the frequencies of the two oscillators. This ratio ρ is called the winding or rotation number of the state and can be either incommensurate (ratio of frequencies an irrational number) or mode locked (ratio of frequencies a rational number with $\rho=P/Q$, P and Q integers). As the coupling between the oscillators or the nonlinearity of the individual oscillators increases, more of the available parameter space is occupied with mode-locked regions. Another common element is that mode locking arises from the nonlinearity of the oscillators; a nonlinear oscillator has an amplitude-dependent frequency and thus can adjust its amplitude in order to mode lock. Many of these general features are captured in the simple one-dimensional map model known as the sine-circle map. This model makes quantitative predictions about the behavior of certain scaling exponents at the critical line of the system (the set of parameter values where chaos first becomes possible). Some of these predictions are local in the sense that they apply only at isolated points on the critical line [4–6] while others are global in that they consider scaling that extends over the entire line [7,8]. The important question to be resolved experimentally is whether or not these predictions are universal; do they apply to any two-frequency system that undergoes mode locking? This has been extensively investigated for the forced nonlinear oscillator by many researchers using different experimental systems [2,3]. Typical techniques used to evaluate the universality class of experimental data are $f(\alpha)$ scaling spectra [9] and power spectra [10,11]. In this paper, we describe a test of universal predictions of the circle map in a system with two internal oscillatory modes. We use a dynamical technique that differs in spirit from previous analysis methods.

Owing to experimental difficulties, experiments involving two intrinsic oscillators [12–14] have received much less attention than forced-oscillator experiments. Two independent oscillators are more complex in principle because each oscillator can adjust to the dynamics of the other; an additional degree of freedom is available. In addition, the size of the radial dissipation is constrained by the physical system and there is no guarantee that the dissipation is large (large dissipation is an assumption implicit in the circle-map theory). In forced systems the unforced state can be adjusted to provide for strong radial damping, thereby ensuring close correspondence with the assumptions of the circle map. Thus the study of two independent oscillators offers a more severe test not only for the universality of the theoretical model but also for the generic nature of the results. In addition to the work presented here and elsewhere [15,16] on two-frequency Rayleigh-Bénard convection, there have recently been other experimental studies of systems with two internal modes with independent frequencies [17,18].

The simple model for quasiperiodicity and mode locking that incorporates universal features at the transition to chaos is the sine-circle map given by the mapping of a circle onto itself:

$$\theta_{n+1}=\theta_n+\Omega-\frac{K}{2\pi}\sin(2\pi\theta_n)\ \ (\mathrm{mod}1)\ . \tag{1}$$

This mapping has two control parameters: Ω, the bare winding number, and K, which represents the nonlinearity or coupling. The basic features are presented here while details can be found elsewhere [4–7]. For $K<1$ this is an invertible mapping; the mapping is single valued for forward and backward iterations. The rotation number

$$\rho \equiv \lim_{n\to\infty}\left[\frac{\theta_n-\theta_0}{n}\right]$$

deviates from Ω, as the nonlinearity K is increased from zero at fixed Ω. In the case of mode locking, ρ takes on the value of some rational ratio P/Q, where P and Q are integers, over a finite interval in Ω.

There are two main features of the circle map in the $\{K,\Omega\}$ parameter space. One is the tongue structure of resonance horns as K is varied. At $K=0$ the irrationals have measure 1 on the unit interval and the rationals, which make up the resonance intervals, have zero measure. For $K=1$ the resonance intervals fill the unit interval and form a fractal set with fractal dimension $d_F=0.870$ [7,8]. The transition to fractal scaling at $K=1$ comes from the development of a cubic inflection point in the circle map. This inflection point also produces universal scaling dynamics at special irrational winding numbers. Any irrationals can be written as an infinite continued-fraction expansion of the form

$$\rho=\cfrac{1}{n+\cfrac{1}{m+\cfrac{1}{r+\cdots}}} \tag{2}$$

where $n,m,r,\ldots$ are integers. This series can be compactly written as $\langle n,m,r,\ldots\rangle$. The special irrationals for universality are those with periodic sequences. The simplest such expansion is for all the terms to be 1, the sequence $\langle 1,1,1,\ldots\rangle$. One can sum this series and obtain the so-called "golden-mean" winding number $\rho_g\equiv(\sqrt{5}-1)/2$. Any winding number which has the same asymptotic expansion of 1's will be termed a golden-mean tail, and the dynamics at that winding number should obey the same predicted scalings. In practice we only use finite truncations of the series, termed golden-mean approximants.

Comparisons between theory and experiment are not always straightforward because, in general, the critical line for a physical system may not be smooth [19–21]. (This does not seem to be as big a problem in forced systems, where the critical line has usually been approximated by a simple curve.) In addition, it is not known how to map the control parameters of any two members of the same universality class, so that the K and Ω of the sine-circle map cannot be easily mapped onto the experimental control parameters. Nevertheless, certain points of the parameter space can be identified, such as the crossings of an irrational winding number region and the critical line. This is the point where the dynamics of the orbit points of the map become chaotic, and for which there are theoretical predictions.

Once the intersection point of the critical line and the irrational winding number have been determined, the comparison between the critical circle-map dynamics and the experiment can be carried out. We cannot directly compare the orbit of an experimental Poincaré section with the orbit of a circle map. What are predicted by universal circle-map theory are coordinate-invariant quantities of the system. It has been shown by Sullivan [22] that the Feigenbaum scaling function [23] is the maximal invariant for a one-dimensional map, of which the circle map is an example. To establish that a certain experimental system is in the same universality class as the sine-circle map, one must determine that experimental invariants agree with those of the theory. This can be done by extracting the scaling function from the experimental data and showing that it agrees with the predicted one. As shown elsewhere [24], the scaling function is extremely sensitive to noise and drift of the control parameters and is difficult to obtain from experimental data (or bad numerics). In this experiment we have succeeded in obtaining the scaling function for a critical Poincaré section.

If the scaling function is not available, a less sensitive test of the universality class of a system is its spectrum of scaling indices, the $f(\alpha)$ curve [9,25]. It can always be obtained from the scaling function, but the reverse is not true. The full thermodynamics of the circle map is well approximated by just two parameters, s_1 and s_2, which can be obtained from products of the scales of the scaling function [26]. This two-parameter approximation to the dynamics of the circle map analytically reproduces the exact thermodynamics to within 1%.

II. EXPERIMENT AND DATA

The experiment consists of a solution of 1.46 mol % ^{3}He in superfluid ^{4}He confined in a small-aspect-ratio convection cell of height 0.80 cm, length 1.60 cm, and width 1.12 cm. The cell (Fig. 1) has upper and lower boundaries of copper and sidewalls of low-thermal-conductance Vespel-22 [27]. Thermal convection is induced by applying a fixed heat current to the top plate while maintaining the bottom plate at fixed temperature. The cell is heated from the top because in solutions of ^{3}He in superfluid ^{4}He the thermal-expansion coefficient is effectively negative; the lighter ^{3}He accumulates at the colder boundary owing to the "heat-flush" effect, thereby producing the unstable density gradient necessary for convection. Near the onset of convection it is believed that a dilute ^{3}He–superfluid-^{4}He mixture is nearly identical to a classical single-component fluid, while far above onset the mixing of the hydrodynamic flow should suppress any contribution due the intrinsic binary character of the mixture. Details and references to these assertions can be found elsewhere [28,29]. In this classical single-component approximation the convective state can be parametrized by two dimensionless numbers: the Rayleigh and Prandtl numbers. The Rayleigh number is proportional to ΔT, the temperature difference across the fluid layer, and is a measure of the drive applied to the system. It is defined as $R=g\beta d^3\Delta T/\nu\kappa$, where g is the acceleration of gravity, β is the effective thermal-

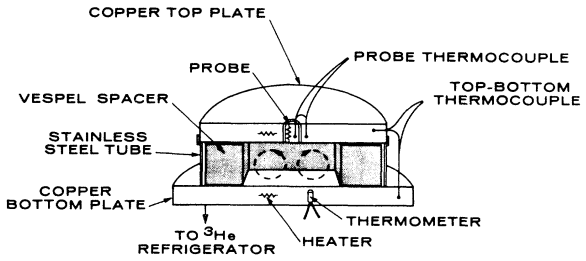

FIG. 1. Low-temperature convection cell.

expansion coefficient, d is the cell height, ν is the kinematic viscosity, and κ is the thermal diffusivity. For time-dependent states above the convective onset the Rayleigh number is time dependent owing to the constant-heat-flow boundary condition at the top plate. Therefore the reported value of Rayleigh number, typically normalized by the critical Rayleigh number $R_c = 2000$, are time-averaged quantities. The other dimensionless parameter in the problem is the Prandtl number $\mathrm{Pr} = \nu/\kappa$. In the ^{3}He–superfluid-^{4}He mixtures Pr is a strong function of the mean temperature T_m and is varied in these measurements over the range $0.06 < \mathrm{Pr} < 0.07$ by varying the temperature over the range $0.83 < T_m < 0.87$ K.

In addition to a global measure of the temperature field from the time dependence of the top-bottom temperature difference, a thermal probe measures a localized region of the flow. Measurement of the dynamics of the system at a single point is adequate to characterize the dynamical state because in small-aspect-ratio convection the sidewalls severely constrain the spatial structure of the fluid flow, leaving only temporal degrees of freedom. A gold-iron thermocouple, whose current is sensed by a superconducting-quantum-interference-device ammeter, measures the local temperature gradient near the center of the cell top plate with temperature sensitivity of 0.3×10^{-7} K $/\sqrt{\mathrm{Hz}}$ [28]. We denote the measured temperature difference at the local probe as $\delta T(t)$. Since we measure temperature differences of the local probe relative to a thermal average over the top plate rather than absolute temperature, there is some rectification of the time series for oscillations that are symmetric with respect to the probe. This leads to an artificial enhancement of the second harmonic of the time series. This is not an intrinsic problem but does produce effects that confuse the interpretation of the data somewhat. To eliminate this problem we filter the data digitally to reduce the large second-harmonic peak.

From the filtered time series the phase-space attractor is constructed using standard dynamical-systems techniques of delay coordinates [30–32] with mutual information determination of the delay [33]. We also construct Poincaré sections as the interpolated intersections of trajectories of the dynamical state with a plane in the delay-coordinate phase space. The location and orientation of the plane is variable so that we can choose sections with the minimum of overlappings and projection singularities which can arise in delay coordinate reconstructions of dynamical attractors. For convenience we normalize the delay coordinates $\delta T(t + n\tau)$ by the size of the attractor so that the new coordinates $X(t + n\tau)$ vary between -1 and 1.

We have made a detailed study of the dynamics and mode locking of two intrinsic modes of thermal convection small-aspect-ratio Rayleigh-Bénard convection in a dilute solution of ^{3}He in superfluid ^{4}He [15,16,34,35]. In the parameter space of Rayleigh number R and Prandtl number Pr regions of different convective behavior exist (Fig. 2). For small R, the fluid conducts heat diffusively. At $R = 2000$ there is a supercritical (continuous) transition to steady convection [28], where the fluid motion is believed to be two convection rolls oriented parallel to the short side of the rectangular convection cell.

The first time dependence begins at the transition to periodic oscillations of frequency f_1. This transition is a forward Hopf bifurcation [36–38] and the onset value depends strongly on Pr. Another Hopf bifurcation at higher R gives rise to a second frequency f_2, incommensurate with the first. This second mode is only weakly interacting with the initial limit-cycle mode, and not until there is a discontinuous transition to a different second mode does measurable mode locking occur. The physical mechanism for this transition is not known. Within a region of parameter space above the discontinuous transition, quasiperiodic (incommensurate frequencies), mode-locked, and chaotic states exist. As in the theoretical model, the state of the dynamics is often well represented by the winding number $W \equiv f_2/f_1$, where f_1 and f_2 are the fundamental frequencies determined from spectral analysis of time-series data. (W is related to ρ in the theory as discussed below). Figure 3 is a typical quasiperiodic time series and power spectrum in which many distinct peaks are observed. Each peak can be written as

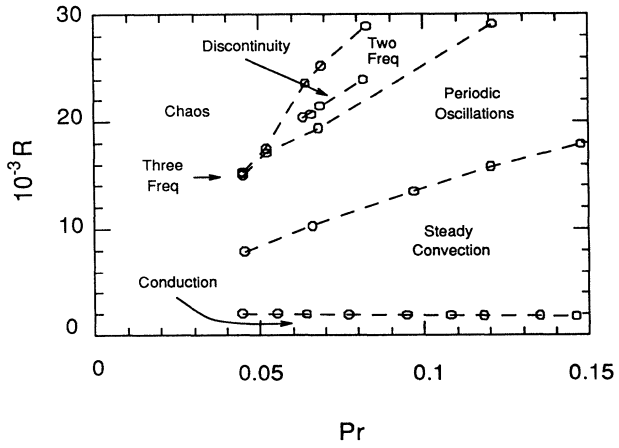

FIG. 2. Phase diagram of convective states in parameter space of the Rayleigh number and the Prandtl number. Regions are described in the text.

a sum, difference, or harmonic of the two fundamental peaks. In Table I the fundamental frequencies and some of the other peaks are compared with the decomposition into combination frequencies. The mode-locking structure know as the "devil's staircase" is constructed from a sequence of such spectra as a function of R at fixed Pr. This structure is illustrated in Fig. 4 for experimental data and is qualitatively similar to the circle-map version. (Note that the range of experimentally accessible winding numbers, $1/8 < W < 2/11$, is substantially less than 1.) By making a series of such measurements at different values of Pr, the locking regions in the $\{R, \mathrm{Pr}\}$ parameter space are determined (Fig. 5). The tongues are seen to broaden as Pr decreases (this is why we plot 1/Pr in Fig. 5) while the value of the winding number is controlled primarily by changing R. A simple qualitative mapping of the control variables R and Pr onto the circle-map variables of K and Ω assigns R the role of Ω and Pr that of $1/K$. In general, one is not guaranteed such a direct relationship and more quantitative comparisons are inadequate.

The boundaries of the regions where quasiperiodic and mode-locked states are observed are higher-dimensional attractors for large R/R_c and the simple quasiperiodic state with no mode locking at smaller R/R_c [15,34,35]. An important characteristic of the theory is the critical line, where certain critical scaling behavior is expected. In the complex experimental parameter space of R and Pr one needs a way to define and locate such a line if it exists. Below we discuss how we accomplish this experi-

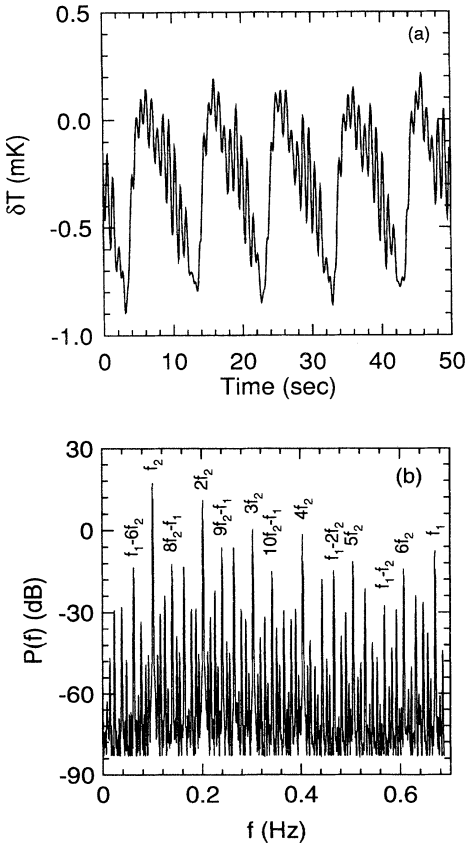

FIG. 3. Quasiperiodic (a) time series of temperature oscillations and (b) corresponding power spectrum. Combination frequencies are labeled in the spectrum.

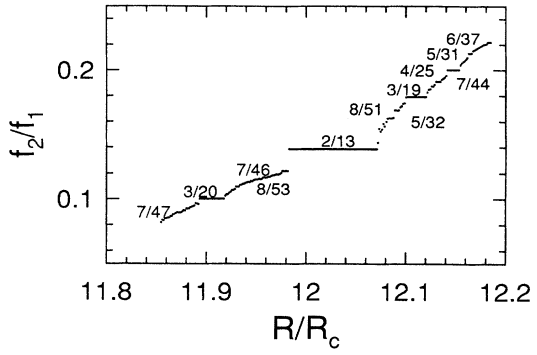

FIG. 4. Experimental devil's staircase of mode-locked intervals for $1/\mathrm{Pr} = 14.9$, slightly above criticality. Prominent lockings are indicated.

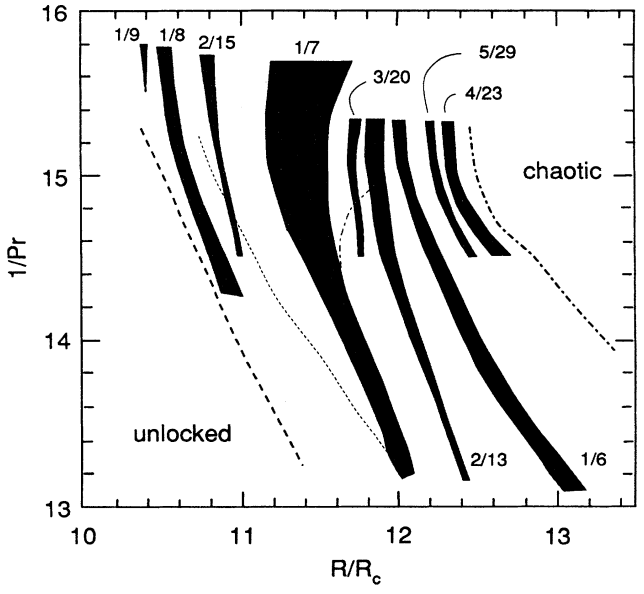

FIG. 5. Experimental regions of mode locking in the 1/Pr and R/R_c parameter space. The dashed lines represent the hysteretic discontinuity at low R/R_c, increasing R/R_c (small-dashed line), and decreasing (large-dashed line), and the transition to high-dimensional chaos at large R/R_c (dash-dotted line). For $1/\mathrm{Pr} \gtrsim 15$, there is structure in the tongues not shown on this global plot.

TABLE I. Quasiperiodic frequency decomposition showing the deduced combination of the fundamental frequencies f_1 and f_2, the measured frequency and the calculated frequency for a given combination.

Combination	f (measured)	f (calculated)
f_1-6f_2	0.062 573 55	0.062 573 58
f_2	0.101 240 70	
$8f_2-f_1$	0.139 908 20	0.139 907 82
$2f_2$	0.202 481 48	0.202 481 40
$9f_2-f_1$	0.241 148 92	0.241 148 52
$3f_2$	0.303 722 00	0.303 722 10
$10f_2-f_1$	0.342 390 28	0.342 389 22
$4f_2$	0.404 962 85	0.404 962 80
f_1-2f_2	0.467 536 36	0.467 536 38
$5f_2$	0.506 203 57	0.506 203 50
f_1-f_2	0.568 775 89	0.568 777 08
$6f_2$	0.607 443 63	0.607 444 20
f_1	0.670 017 78	

mentally. First we describe simple quasiperiodic and mode-locked dynamics that occur in a region of parameter space in our fluid system that is far below criticality.

One can construct the dynamical state of a system composed of two nonlinear, interacting modes of oscillation in a three-dimensional phase space consisting of normalized delay coordinates $X(t+n\tau)$ of the local-probe-temperature oscillations. The trajectories in this phase space lie on a manifold that is topologically equivalent to a two-dimensional torus (in practice the torus is often quite distorted). To better understand the dynamics one constructs a two-dimensional mapping (Poincaré section) of the plane by plotting the interpolated intersections of system trajectories with a two-dimensional surface. We use a planar surface oriented in such a way as to produce the "best" mapping, i.e., one that avoids crossings, kinks, etc. In this way we can avoid distortions due to the imperfect embedding of delay coordinate schemes [30–32].

Note that our method of generating a Poincaré section is more general than the stroboscopic technique used in forced oscillator experiments. In the subcritical regime, this Poincaré map will form a smooth one-dimensional curve diffeomorphic to a circle. In Fig. 6 an example is shown for experimental data in which the dynamical state is very close to a period-2 resonance. A one-dimensional return map is constructed by parametrizing the iteration of points on the circle by an angular coordinate θ, producing a circle map θ_{n+1} as a function of θ_n [Fig. 7(a)]. The rotation number of this Poincaré section is different from W obtained from the frequency spectrum because of the ambiguity in choosing the plane of the Ponicaré section that cuts the torus. It is operationally easier to produce a section by cutting through the minor axis of the torus, thereby producing a rotation number ρ that is related to W by $\rho=1/W$ mod1. The state represented in Figs. 6 and 7 has $W\approx 2/13$ corresponding to $\rho\approx 1/2$. In this and all future Poincaré sections we shall refer to ρ as the appropriate winding number. To illustrate the tangent bifurcation structure of mode locking we plot in Fig. 7(b) the second-iteration map for the data in Fig. 6, for which the dynamics is close to a period-2

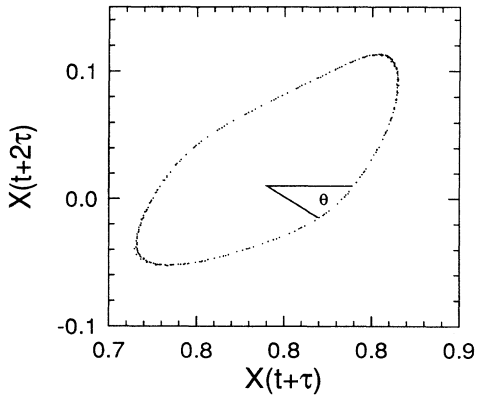

FIG. 6. Experimental Poincaré section in delay coordinate phase space (units normalized to the size of the attractor). Angle θ indicates the parameter for generation of the return map.

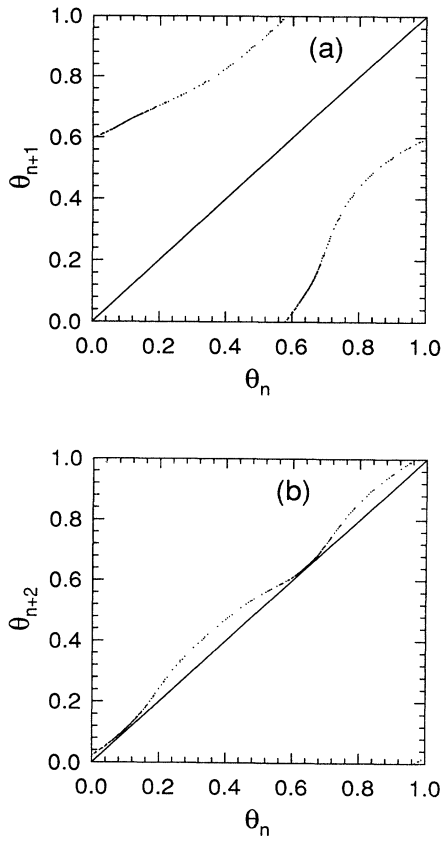

FIG. 7. Return maps for (a) first iteration θ_{n+1} vs θ_n and (b) second iteration θ_{n+2} vs θ_n for experimental data near locking to a period-2 resonance.

locking. (For a period-q locking a tangent bifurcation will occur in the qth iterate map.)

III. TRANSIENT DATA AND ANALYSIS

A major problem in experiments on quasiperiodicity and mode locking with two intrinsic frequencies is how to define the critical line in the real experimental parameter space. In the circle map, criticality comes about when the map becomes noninvertible at a cubic inflection point. In the more general case of a two-dimensional map one can think of criticality as resulting from a loss of smoothness or differentiability of the invariant circle as, in general, the return map will not have a cubic inflection point on this critical line [21,39]. A theoretical approach for determining the critical line [19,20] was based on the structure of the stable and unstable manifolds of the periodic points in the interior of a resonance horn [5,40]. At the edges of a locking the periodic points arise from a saddle-node bifurcation (the two-dimensional phase-space version of the tangent bifurcation) and thus the stable manifold must be characterized by two real eigenvalues (Flouquet multipliers); see Fig. 8(a). If somewhere in the interior of the horn the periodic points take on spiral stability, ie., complex-conjugate eigenvalues, then the stable manifold is no longer differentiable at those points; see Fig. 8(b). Other mechanisms can also lead to a loss of smoothness of the circle, as discussed in Refs. [5,19,40], but for simplicity we define our critical line to consist of the minima of the spiral stability regions. Other criteria based on the qualities of the time series at the golden mean are often used, but our technique provides an independent measure of criticality. To realize this method the linear stability of the periodic points has to be determined. This requires analysis of the system's transient relaxation to the attracting periodic points. Therefore, we turn our attention to the production and analysis of transients in real physical systems with many potential degrees of freedom.

In simple systems such as electronic oscillators it is easy to produce transients because one can specify the initial conditions with a small number of parameters. On the other hand, systems described by partial differential equations have spatial degrees of freedom and require specifying initial conditions at every point in space. This is impossible experimentally for arbitrary initial conditions, and so one typically uses another stable state of the system as the initial state and produces transients by making sudden changes in a control parameter. An important point to note here is that even if the long-time dynamics of the system are low dimensional, as in our experiments on quasiperiodic convection, a sudden change in control parameter is likely to induce dynamics in a higher-dimensional phase space. These higher-dimensional motions should damp out more quickly than low-dimensional transients of interest, but there is often a mixing of time scales, which complicates interpretation of the dynamics. With that caveat, we describe cases where the interpretation is straightforward and quantitative results obtainable.

Consider transient relaxation to a single periodic point in a period-2 cycle. This means that we take every other iterative point from a Poincaré section of the mode-locked state. (The axes of Poincaré sections shown in this paper are proportional to the temperature oscillations of the local probe but are scaled so that the entire range of the attractor is ± 1.) The data in Fig. 9 are for a state with spiral stability for which the real and imaginary parts of the complex-conjugate eigenvalues λ_R and λ_I can be defined by considering the position of the points relative to the asymptotic stable state: $\mathbf{r}(r,\theta,n)=\mathbf{r}_0 e^{-\lambda_R n + i\lambda_I n}$, where n is the discrete-time iterative variable. λ_R is obtained by plotting $\ln r$ versus n as in Fig. 10(a). Likewise the angular rotation is just the slope of θ versus n [Fig. 10(b)]. We get $\lambda_R = 0.18$/iteration and $\lambda_I = 1.7$ rad/iteration. In the region of the resonance horn where two real eigenvalues govern the stability of the periodic points, one eigenvalue

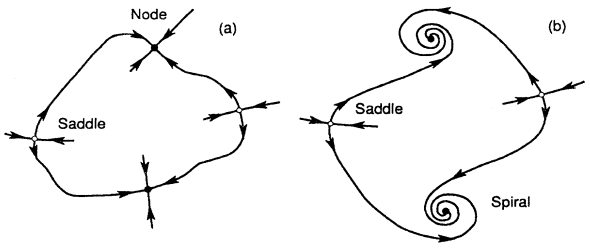

FIG. 8. Stable and unstable manifolds: (a) of saddle node and (b) of spiral periodic states. Saddles are denoted by (○) and attracting periodic points by (●).

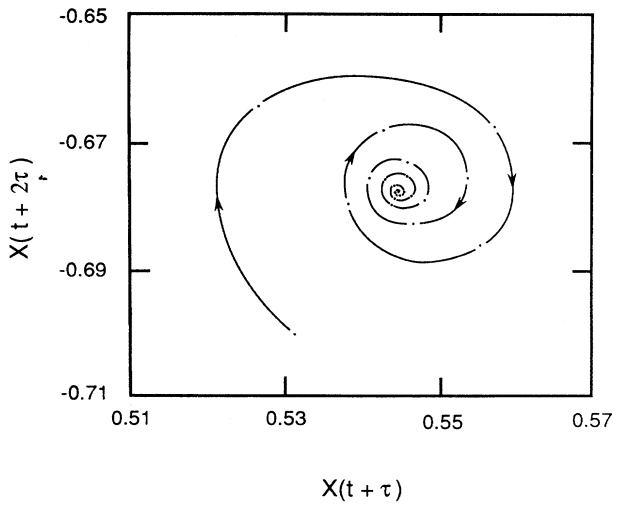

FIG. 9. Transient Poincaré section showing a spiral approach to a periodic points in the 2/13-resonance horn; $R/R_c = 12.025$ and $1/\mathrm{Pr} = 14.77$. Solid curves are a guide to the eye and not system trajectories.

is typically much larger than the other and only the smaller one is accessible to experimental measurement. An example of pure radial relaxation is shown in Fig. 11 where we get $\lambda_R = 0.3$/iteration. By making a series of such measurements across the 2/13 resonance, we can specify the stability of the periodic points inside that tongue. In Fig. 12, λ_R and λ_I are shown for $\mathrm{Pr}^{-1} = 14.77$, where spirals exist over most of the horn, and for $\mathrm{Pr}^{-1} = 14.56$, where there are no spirals. Notice how the radial eigenvalue decreases towards the middle of the locking for the spiral case but is peaked for the nonspiral data. Similarly the approximate threshold for spirals is determined for the 3/19 and 4/25 resonances. The accuracy with which this upper boundary to the critical line can be determined decreases as the cycle length increases. Another limitation is that as the two real eigenvalues become close in magnitude, as they must before the transition to spiral stability, it becomes difficult to resolve the spiral component before the transient has decayed to the noise threshold.

The critical line, determined by this stability constraint and by the condition that the critical line is below any tongue hysteresis, is placed slightly below the locus of apparent spirals. The tongue diagram, the spiral region of the 2/13 resonance, and the critical line are shown in Fig. 13. The general shape of the critical line follows Ref. [19]. Also illustrated are lines of constant winding number with asymptotic golden-mean expansions. These are defined as $\rho_g^{(n)} = \langle n, 1, 1, 1, \ldots \rangle$ according to (2). It is at the intersections of these golden-mean lines and the critical line that universal predictions of the sine-circle-map model should apply. In the next section we describe those predictions and the analysis tools for making quantitative comparisons between theory and experiment.

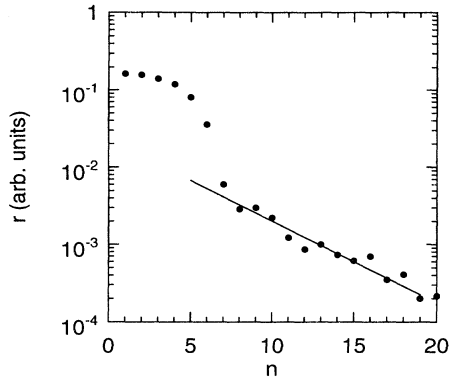

FIG. 11. Radius r vs iteration n for experimental data with pure real eigenvalues. Only the smaller eigenvalue is measured by the fit to the data (——).

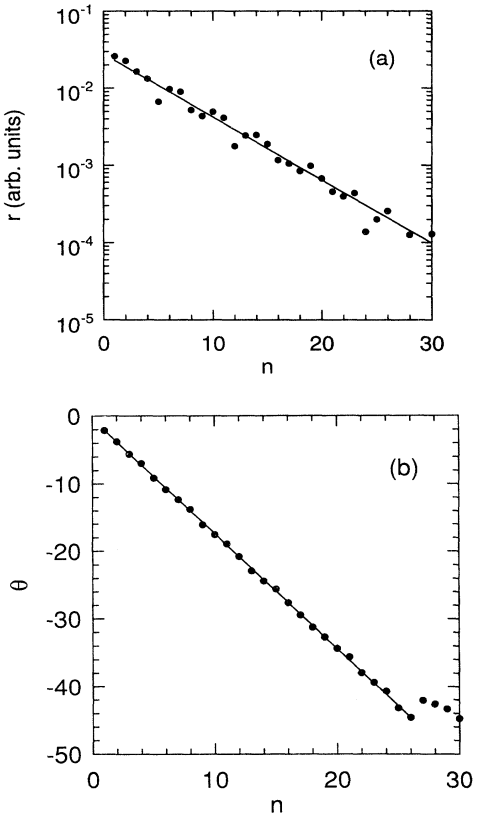

FIG. 10. Plots of (a) r and (b) θ vs iterate number n for data from Fig. 9. Solid lines are straight-line least-squares fits to the data where the slope determines the eigenvalues λ_R and λ_I.

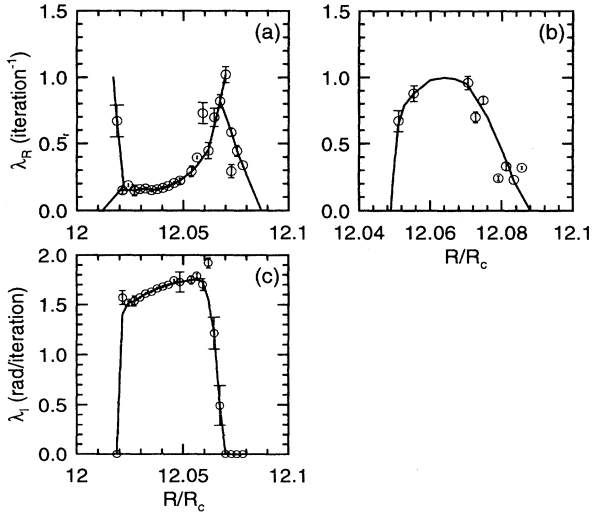

FIG. 12. Eigenvalues for periodic points (Floquet multipliers) across the $W = 2/13$ locking interval: (a) λ_R vs R/R_c, $1/\mathrm{Pr} = 14.77$; (b) λ_R vs R/R_c for $1/\mathrm{Pr} = 14.6$; (c) λ_I vs R/R_c for $1/\mathrm{Pr} = 14.77$. Lines are a guide to eye and error bars reflect statistical uncertainty in the fits.

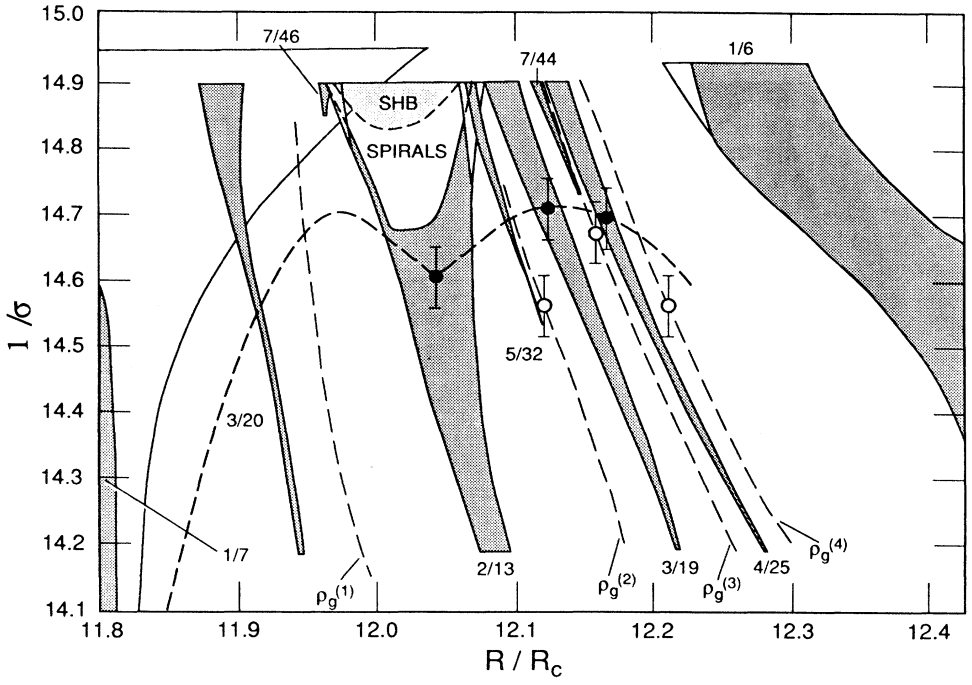

FIG. 13. Resonance horns in parameter space of inverse Prandtl number 1/Pr and normalized Rayleigh number R/R_c. Dashed vertical lines trace golden-mean lines with winding numbers $\rho_g^{(1)}$, $\rho_g^{(2)}$, $\rho_g^{(3)}$, and $\rho_g^{(4)}$. Lightly shaded regions indicate hysteresis; the interior structure of the 2/13 resonance consists of stable spiral periodic cycles and secondary Hopf bifurcations (SHB) of the periodic cycles. Also shown are the estimated locations of the critical line (— — —) from analysis of spiral periodic cycles (○) and of $f(\alpha)$ spectra.

IV. MULTIFRACTAL ANALYSIS

Multifractal analysis is the method used to compare experimental data with predictions from the circle map. We perform several different comparisons in increasing order of sensitivity: we compare the ordering of the orbit points along the Poincaré section; the scaling of singularities, $f(\alpha)$; and the scaling function $\sigma(s)$. All of these tests rest on the extraction of time-ordered segments (described in Sec. IV A) from an experimental Poincaré section. Because the method we use to compute the spectrum of singularities requires an understanding of the scaling function, we invert the order of presentation, introducing the scaling function in Sec. IV B and the scaling spectrum in Sec. IV C.

A. Scaling segments

The basis for the analysis of the data is the partition of the points in the Poincaré section into a set of segments that form a one-dimensional curve. For a map of the circle onto itself, the exact ordering of the orbit points along a curve is determined by the winding number. The ordering can be used to determine the winding number and to check the one-dimensional character of the manifold. The winding number obtained by this technique is more sensitive to noise and drift in the control parameters than the one obtained directly from the power spectrum.

An approximate winding number can be obtained by calculating, for a certain number of orbit points, how many times the orbit goes around. Normally for a loop one would expect that a "center" has to be found and the total angle of rotation of a radius determined. This is not always possible, as some of the loops may be distorted with no clear center. An alternative method, which is independent of the embedding of the loop, is to consider the local turning of the orbit as it traces the loop. By summing the angle differences between the displacement vectors and dividing by the total radians in a full turn, we obtain the number of times t that the orbit has gone around,

$$t=\frac{1}{2\pi}\sum_k \cos^{-1}\left[\frac{(x_k-x_{k-1})(x_{k+1}-x_k)}{\|x_k-x_{k-1}\|\|x_{k+1}-x_k\|}\right], \qquad (3)$$

where $\cos^{-1}$ is the angle between 0 and 2π determined from the relative positioning of the displacement vectors in the argument.

In the experiment the orbits never actually close, and the period is inferred from the number of iterations required to return to the neighborhood of an orbit point—the close-return times. If an orbit point lands sufficiently close to another orbit point we assume that they are the same point up to the measurement errors in the experiment. The period is determined by choosing a random

set of initial points and determining points that come closer and closer to this set. Different initial points will have different sets of close-return times, but if the orbit is close to a periodic one there will be a few common close-return times that are all candidates for the period of the orbit. These can be tested by verifying the winding number of the orbit.

The ordering of the points of a periodic orbit of a monotonic map of the circle can be determined from the denominator and the numerator of its rational winding number. If the winding number is P/Q, there are Q points of the orbit along the circle. Each iteration of the map takes the orbit P points along the circle, either clockwise or counterclockwise, so that the next point in time is not the closest one with respect to coordinates. To determine the closest point in coordinate space one has to determine the closest-return time r. If at each step the orbit moves P points along the curve, then there is a minimum number r of P steps that must be taken to land exactly one point from the starting one. The close return time r can be determined by finding the solution to the equation

$$rP = 1 \ (\mathrm{mod} Q) \tag{4}$$

in the range $1 \le r \le Q-1$. If the winding number of an orbit is 8/13, then the close return time r is 5 as $5\times 8 = 40 = 1+3\times 13$.

Once the close-return for a given orbit is determined, its winding number can be verified. This is done by connecting each of the Q orbit points x_n to their nearest neighbor in coordinate space, that is, connecting the point x_n to x_{n+r}, where r is the close-return time for the P/Q orbit (see also Glazier, Gunaratne, and Libchaber [41]). If the winding number is not correct, then the connected points will not form a smooth one-dimensional manifold. An example of the determination of the winding number of an experimental orbit is given in Fig. 14. In Fig. 14(a) the set of orbit points used in Figs. 14(b) and 14(c) are not connected. In plot (b) the winding number was assumed to be 31/143 with the corresponding close return time being $r=60$; in plot (c) the winding number was assumed to be 30/143 with $r=62$. In (b) the correct choice was made for the winding number. By exploring nearby rotation numbers (those that have the same initial

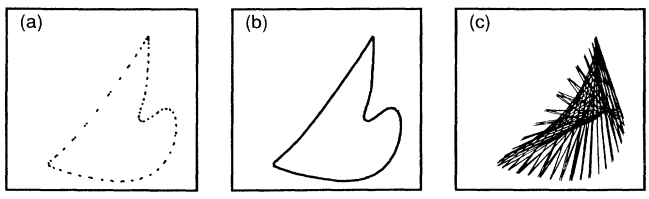

FIG. 14. Given a winding number P/Q, each orbit point x_n of (a) is connected to supposed close return, x_{n+r} [see Eq. (4)]. If the winding number is correct, (b) is obtained, and if chosen incorrectly, (c) is obtained.

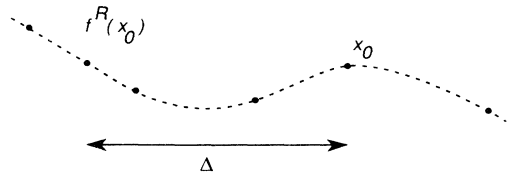

FIG. 15. The end points of a segment Δ_k are determined from x_k and its close return time $f^r(x_k)$. The length is computed by joining all points that are within the end points of the segment. This is a better approximation to the smooth manifold.

sequence in the continued-fraction expansion) one can determine that the rotation numbers are accurate to within a few parts per thousand, and not parts per hundred as one would expect from an orbit of period 143. The procedure described for the computation of the winding number requires less data for comparable accuracy than the one described in Stavans, Thomae, and Libchaber [42] because it uses the ordering of the points.

The segments from which the thermodynamics is derived are the segments Δ_k that connect neighboring points x_k to x_{k+r} along the manifold in coordinate space. In some cases there are more points in the data set than are needed for the orbit, and the extra points can be used to determine a smoother approximation to the manifold (a loop), as indicated in Fig. 15.

B. Scaling function

The scaling function (introduced by Feigenbaum in Ref. [43]) gives complete details on how the orbit points are being positioned along the loop. It give asymptotic information relative to a few initial orbit points in a small region of the loop, and completely characterizes the circle-map universality class.

For the purpose of computing scaling functions it is necessary that the winding number be a periodic continued fraction, in our case a series of 1's forming a golden-mean tail. If the winding number determined from the data is not a golden-mean tail, then there are at least two options. One can consider the longest possible sequence of 1's in the actual winding number. For example, if the winding number is $28/129 = \langle 1,4,1,1,1,1,5 \rangle$, then the longest sequence would be $\langle 1,4,1,1,1,1 \rangle$, which corresponds to the winding number 5/23. The first 23 points of the longer orbit would be used as the end points for the segments, using the remaining points to determine intermediate points within the segments. Alternatively, one can reconstruct the behavior of the map as a function of the control parameters in the vicinity of a golden-mean-tail point, and from the reconstructed map determine the scaling function [24].

With the reconstruction technique one can utilize all of the available data, even if the winding number is not exactly a golden-mean tail. Naively, one would expect that in an orbit of winding number 28/129, as above, one could use the nearest golden-mean approximant with

smaller denominator, 21/97. However, in the sine-circle map, if the 28/129 orbit is compared to the 21/97 orbit, one finds that the first 23 orbit points of the orbits are in close agreement, and after that the phase difference between the two orbits can amount to errors of up to 20%. To eliminate this phase problem we choose two data sets with different winding numbers: one smaller than the golden-mean-tail approximant, and one larger. The return map of the two data sets is used to interpolate new return maps, and the one with the correct winding number (21/97) is chosen for computing the segments. The interpolation procedure amounts to small changes, as the two return maps cannot be distinguished from each other on a plot [24]. As a check to the reconstruction technique, we have computed the value of δ, the eigenvalue that controls the scaling of tongue widths, to be 2.8 (to be compare with the prediction of 2.83). We use the reconstruction technique in determining the scaling function.

The determination of the scaling function for an arbitrary rotation number requires a set of segments organized as in Fig. 16. The points in the figure correspond to a rotation number of 8/13, a golden-mean approximant. The same orbit is viewed as determining different sets of segments, each set containing a Fibonacci number of segments organized in a level. The actual end points of the segments can be expressed directly in terms of the orbit points. The end point for a segment $\Delta_k^{(n)}$ is a function of the level n, for example, $\Delta_0^{(1)}$ has as end points x_0 and x_2, whereas $\Delta_0^{(2)}$ has as end points x_0 and x_3. For the golden-mean approximants the end points for all intervals can be expressed in terms of the Fibonacci numbers, and similar expressions hold when the rotation number is a golden-mean tail.

The general rule for determining the segments is to choose an initial segment $\Delta_0^{(n)}$ and iterate it with the map, so that if we know the end points of $\Delta_0^{(n)}$ we then know the end points of all other segments. The end points of $\Delta_0^{(n)}$ are given by x_0 and x_{r_n}, where r_n is determined from the p_n/q_n winding number as in Eq. (4). At level n there will be F_n segments, F_n being the Fibonacci sequence obtained from the initial values $F_0=1$ and $F_1=2$. The scaling function is composed from a series of piecewise constant steps of height $\sigma_t^{(n)}$ placed in ascending order t to approximate the function

$$\sigma(s)=\lim_{n\to\infty}\sigma^{(n)}_{\lfloor sF_n\rfloor}\ , \tag{5}$$

where s ranges between 0 and 1, and $\lfloor x\rfloor$ is the largest integer smaller than x. The scaling $\sigma_t^{(n)}$ is given by the ratio between $\Delta_t^{(n+1)}$ and its parent segment:

$$\sigma_t^{(n)}=\frac{|\Delta_t^{(n+1)}|}{|\Delta^{(n)}_{\Theta(t,F_n)}|}\ , \tag{6}$$

where F_n is the Fibonacci number of segments that exists in level n. The function $\Theta(t,F)$ is the parent index function, which in the simple case of the golden mean returns $t-F$ if $t\geq F$ and t otherwise. For any golden-mean-tail winding number, the segments are arranged exactly as in Fig. 16, and $\Delta_0^{(n)}$ is the segment between x_0 and x_{q_n}. The general formulas for the segments in the scaling ratios are worked out in a binary Fibonacci base in the Appendix.

The scaling function $\sigma(s)$ determines the asymptotic ratio between the two segments that are separated by a fraction s of the periodic orbit. For smaller values of s the initial segment gets mapped around the loop a smaller number of times than for larger values of s. We should then expect that the errors in the scaling function will be larger for larger values of s.

In Fig. 17 we have plotted two different scaling func-

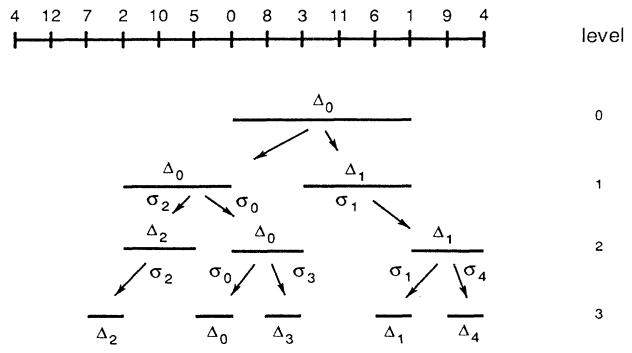

FIG. 16. Tree structure of the segments.

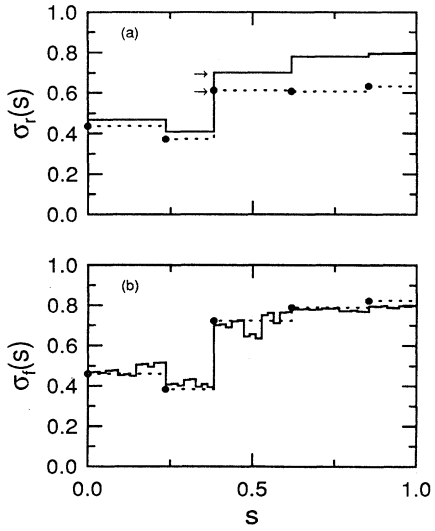

FIG. 17. Scaling functions for the experimental data. The theoretical curve is solid and the experimental curve is dotted. In (a) the scaling function was computed directly from an orbit that approximated a golden-mean-tail winding number; for short periods of time the approximation is good, but decreases for longer periods. In (b) the scaling function was corrected for phase problems and averaged between two regions. Only the difference in the major jumps must be compared, as indicated.

tions computed from the experimental set. One of the curves [Fig. 17(a)] was obtained directly from the data set, whereas the other curve [Fig. 17(b)] was obtained from the reconstruction process. In comparing these curves with the theoretical prediction one should compare the sequences of ups and downs and the initial part of each of the steps, as these remain unchanged when the number of steps in the scaling function is increased. In Sec. IV C we will compute the spectrum of singularities $f(\alpha)$ from this scaling function and directly from the segments on the loop.

C. Thermodynamics

Even though the scaling function is the maximal invariant for the maps of the universality class of the sine-circle map, there are other invariants that can be computed. One class of invariants, introduced by Sinai [44] and Bowen [45] and later generalized by Ruelle [46], closely follows the formalism of thermodynamics. The analogy is found when we try to compute the Hausdorff dimension of the set covered by the segments Δ_k of size $|\Delta_k|$. To determine the Hausdorff dimension β_H one determines the value of β such that the sum

$$Z(\beta)=\sum_k |\Delta_k|^\beta \tag{7}$$

is neither zero nor infinity in the limit of infinitely small segments. One notices that if the segments Δ_k are taken to be the Boltzmann factors and the Hausdorff exponent is taken to be the inverse temperature β, then the sum (7) can be considered to be the partition function of a system where the "energy" of the state k is given by $-\ln|\Delta_k|$.

If the number of segments $\Delta_k^{(n)}$ at a certain level n is Q_n, then the "pressure" $p(\beta)$ can be defined as the limit

$$p(\beta)=-\lim_{n\to\infty}\frac{1}{\ln Q_n}\ln\sum_{0\le k<Q_n}|\Delta_k^{(n)}|^\beta , \tag{8}$$

where for golden-mean-tail winding number Q_n grows as ρ_g^n as n goes to infinity, ρ_g being the golden mean $(\sqrt{5}-1)/2$. The choice of the name pressure for this quantity was introduced by Ruelle in analogy with the lattice-gas quantity. From it several other quantities of interest can be derived: the spectrum of singularities $f(\alpha)$ and related quantities α and τ [47] and the generalized dimensions D_q [48]. These quantities are functions of the pressure p and its derivative with respect to β, which we denote by u, the internal energy.

To establish the relationship between the spectrum of singularities and the pressure, we must recast the definition of the spectrum of singularities in terms of the segments Δ_k. The $f(\alpha)$ formalism assigns to each segment Δ_k a probability p_k (in general the probability of the segment being visited). One then considers the sum

$$\Gamma(q,\tau)=\sum_k\frac{p_k^q}{|\Delta_k^{(n)}|^\tau} . \tag{9}$$

Because the segments Δ_k were defined as being equiprobable, we can take $p_k=1/Q_n$. The definition of $f(\alpha)$ is given in the limit of $|\Delta_k|\to 0$ for all k. In that case, for a fixed q the sum Γ is either zero or infinity except for a particular choice of τ, which then defines the function $\tau(q)$. From the τ function one introduces the conjugate variable $\alpha=\partial_q\tau$, and the Legendre transform of τ, the spectrum of singularities $f=q\alpha-\tau$. By comparing the sum in (9) with the partition sum in (8) we can establish the correspondence (see Feigenbaum [49])

$$q=-p(\beta) \quad \text{and} \quad \tau=-\beta . \tag{10}$$

By implicit differentiation of these relations we obtain the expression for α, as

$$\alpha^{-1}=u(\beta)=\frac{\partial p(\beta)}{\partial\beta}=-\lim_{n\to\infty}\frac{1}{\ln Q_n}\frac{\sum_k|\Delta_k^{(n)}|^\beta\ln\Delta_k^{(n)}}{\sum_k|\Delta_k^{(n)}|^\beta} . \tag{11}$$

Notice that to evaluate this expression from the segments there is no need to perform a numerical differentiation of $\tau(q)$, as it is given in terms of the segments. The expression for the singularity spectrum is then

$$f(\alpha)=\beta-\frac{p(\beta)}{u(\beta)} . \tag{12}$$

The relationship between the pressure and the generalized dimensions also follows from the sum in (9). Taking as the definition of the generalized dimension D_q the relation $\tau=(q-1)D_q$, we get

$$D_q=\frac{\beta}{1+p(\beta)} . \tag{13}$$

With the above expressions one can determine the spectrum of singularities and the generalized dimensions in terms of the parameter β. In practice one fixes a value of β and from the set of segments the pressure $p(\beta)$ and the energy $u(\beta)$ are computed using expressions (8) and (11). With these two values all other quantities are given implicitly [24]. A similar approach for computing the $f(\alpha)$ spectrum was discussed by Chhabra *et al.* [50,51].

The thermodynamic quantities can be directly obtained from the scaling function. The connection is established by evaluating the asymptotic behavior of each segment. Every segment at a given level can be written as the product of scalings at previous levels multiplied by the initial segment. For example, $|\Delta_4^{(3)}|=\sigma_1^{(1)}\sigma_1^{(2)}\sigma_4^{(3)}|\Delta^{(0)}|$. The value of a given $\sigma_k^{(n)}$ converges to a limit exponentially fast as a function of n, so for the thermodynamics, $\sigma_k^{(n)}$ (for any n) can be substituted for its asymptotic values. Using the five-step approximation to the scaling function, all segments beyond level 2 can be written as products of the several scales σ_k and three initial segments $\Delta_k^{(2)}$.

One can verify that the partition function (8) is given by a power of a transfer matrix T as

$$Z^{(n)}(\beta)=[1,1,1]T^{(n-2)}(\beta)[|\Delta_0^{(2)}|^\beta,|\Delta_1^{(2)}|^\beta,|\Delta_2^{(2)}|^\beta]^\dagger , \tag{14}$$

where $T(\beta)$ is the matrix

$$\begin{bmatrix} \sigma_0^\beta & \sigma_1^\beta & 0 \\ 0 & 0 & \sigma_2^\beta \\ \sigma_3^\beta & \sigma_4^\beta & 0 \end{bmatrix} . \quad (15)$$

In the limit of large n, the partition function (14) is dominated by the largest eigenvalue $\lambda(\beta)$ of $T(\beta)$, and the pressure can be written as

$$p(\beta) = -\frac{1}{\ln \rho_g} \ln \lambda(\beta) . \quad (16)$$

In the circle map there is the extra constraint that the Hausdorff dimension of the orbit be equal to 1. The Hausdorff dimension is the generalized dimension D_0, which implies that the pressure $p(\beta_H)$ is zero from Eq. (10), and that as $D_0 = 1$, the value of β_H is one from Eq. (12).

We can incorporate the constraint directly into the evaluation of the largest eigenvalue, as it is also satisified experimentally. Defining $z = 1/\lambda$, we get the secular equation $1 - z\sigma_0^\beta - z^2(\sigma_2\sigma_4)^\beta - z^3[(\sigma_1\sigma_2\sigma_3)^\beta - (\sigma_0\sigma_2\sigma_4)^\beta] = 0$. From the condition $p(\beta = 1) = 0$ we have $z = 1$ for $\beta = 1$ and we get the simplified expression

$$(1 - z s_1^\beta)(1 - z^2 s_2^\beta) - z^3(1 - s_1)^\beta(1 - s_2)^\beta = 0 , \quad (17)$$

where $s_1 = \sigma_0$ and $s_2 = \sigma_2\sigma_4$ [26]. The final secular equation depends on only two parameters, s_1 and s_2, whereas the original scaling function had five parameters. This indicates that the thermodynamics of the circle map is degenerate in the sense that there are many different scaling functions (and therefore many different dynamics) that produce the same thermodynamics [49]. The theoretical spectrum of scalings $f(\alpha)$ can be determined from just the two parameters $s_1 = 0.468$ and $s_2 = 0.556$ to within plotting accuracy (around 1%).

D. Computing the thermodynamic quantities

In this subsection we explain some of the practical details involved in computing the thermodynamic quantities from the experimental data. Most of the difficulties come from the finite number of segments. For a fixed number of segments there is only a finite range of the parameter β that can be used reliably, and outside this range the partition function (8) is dominated by a single segment. To circumvent this problem we have used a combination of scaling-function techniques and direct methods that utilizes all the data available.

To perform a multifractal analysis of the orbit, it must be first verified that the orbit is generating a scaling object. This is done in two different ways: with the scaling function and by direct computation of the partition function. The scaling-function method consists of verifying that the points are indeed being placed along the loop as a circle map, and assuming that this persists for all scales. This need not be the case in a two-frequency system like the one being studied. Next the scaling is checked by computing the scaling function, as presented in Sec. IV B. The direct method consists of computing the partition function (8) and verifying that it grows exponentially as the number of segments is increased. The growth is plotted in a log-log plot in Fig. 18 for three different values of β. This plot verifies directly from the data that the limit used to compute the pressure (10) does exist. As smaller segments are better converged than larger ones [the error term for the largest segment goes as $(1.288\,57\ldots)^{-\ln Q_n}$], the scatter in the data for negative values of β is smaller than for positive β.

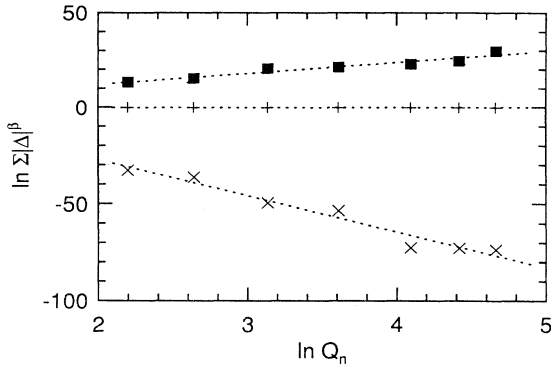

FIG. 18. Scaling of the partition function, Eq. (7), with the cycle length Q_n. Three different values of β are used: $\beta = -10$ (■), 0 (+), and 10 (×).

A straightforward evaluation of the $f(\alpha)$ curve for the small number of data points that we have here, of order 100, gives reasonable spectra. For example, the maximum of the $f(\alpha)$ curve is at 0.99 ± 0.01, indicating that the fractal dimension of the orbit is consistent with 1. But the procedure is not robust and is strongly affected by a few segments. In particular the largest and smallest segments dominate the determination of the range of scales, i.e., the values of $\alpha_{\max}$ and $\alpha_{\min}$. This is because these quantities depend on the interval sizes raised to the power β and thus the largest segment dominates the sum for large positive β, whereas the smallest segment dominates for large negative β. In Fig. 19 we illustrate this

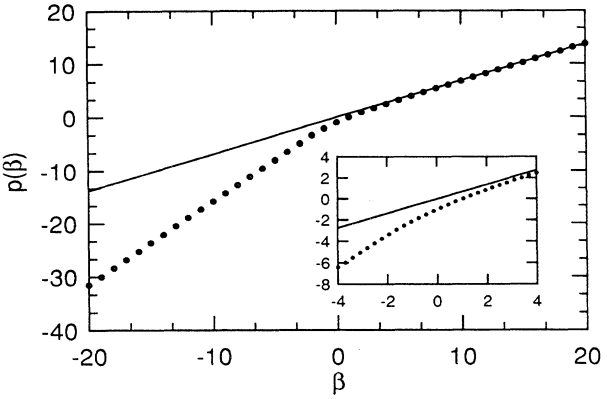

FIG. 19. $P(\beta)$ vs β for experimental data. For (●) all the data were used and for (——) only the largest segment was used.

for large segments by plotting $p(\beta)$ for all the data and comparing it with $p(\beta)$ computed from only the largest segment; for $\beta > 8$ (which corresponds to $\alpha \cong 1.5$) there is no difference between the two. This indicates serious problems since it is necessary to have good values of $p(\beta)$ for $\beta > 30$ to accurately obtain $\alpha_{\max}$.

To quantify the effects of the smallest and the largest segments, we have plotted the energy function, Eq. (11), as a function of β. The plot is reproduced in Fig. 20 and except for a small region around $\beta=0$ the function assumes only two values:

$$u_{\min} = -\frac{1}{\ln Q_n} \ln |\Delta_{\max}^{(n)}| , \quad u_{\max} = -\frac{1}{\ln Q_n} |\Delta_{\min}^{(n)}| . \tag{18}$$

The transition region is where all the segments are contributing to the partition sum. Given that the spectrum of singularities can be well determined by just the two parameters s_1 and s_2, we can directly compute $p(\beta)$ for the transition region and use it to fit the values of s_1 and s_2. Then, for illustration, the spectrum of singularities (or any other thermodynamic quantity) can be computed from them.

To determine the parameters s_1 and s_2 we have fitted the thermodynamic pressure obtained directly from the segments in the Poincaré section with the expected expression (10). The fit is done in a limited range of values of the parameter β (which plays the role of temperature) to avoid the dominance of the partition sum (8) by a few segments. The range of β to be used may seem arbitrary at first, but can easily be extracted from the plots of the "energy" u as a function of the parameter β. The energy has a sharp transition around $\beta=0$ and choosing a range of β around the transition assures that none of the segments is dominant in the partition sum (8).

The fit is computed using a nonlinear least-squares fit, and the fit is done many times using different collections of values of the pressure $p(\beta)$, with a bias towards negative β (which represents the better-converged values). By repeating the fit many times we are able to determine a distribution for the values of the parameters s_1 and s_2, from which the fitting errors are determined. In Fig. 21 we plotted the set of points for the pressure and the curve obtained from the fitted values: $s_1 = 0.47 \pm 0.01$ and $s_2 = 0.61 \pm 0.2$. The $f(\alpha)$ spectrum obtained using these parameters is shown in Fig. 22. Also shown for comparison is a subcritical $f(\alpha)$ curve. In principle, a subcritical data set is not multifractal and should collapse to a point. Finite-size effects, however, associated with finite cycle approximations to the golden mean cause some residual multifractal scaling (see Arneodo and Holscneider [52]) and a narrow but finite width curve (see also the examples in Glazier, Gunaratne, and Libchaber [41]).

From the quantities s_1 and s_2 we can calculate the value of the inflection point exponent which characterizes

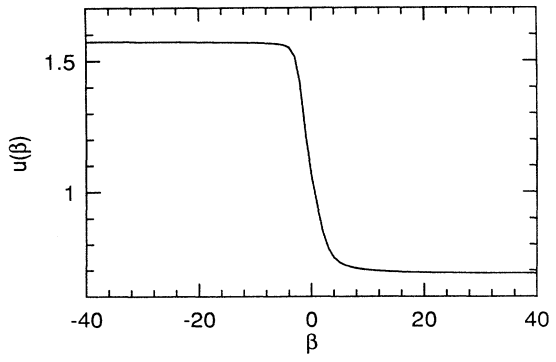

FIG. 20. Energy function for the experimental data. Due to a finite number of segments, the smallest and the largest segments dominate the function at the extremes of the β parameter range.

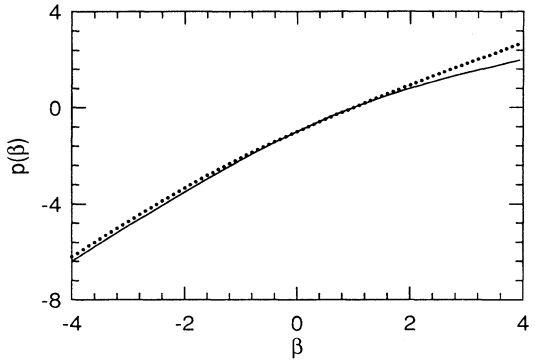

FIG. 21. Fitting of the pressure. The points represent the data and the solid curve the fitted pressure.

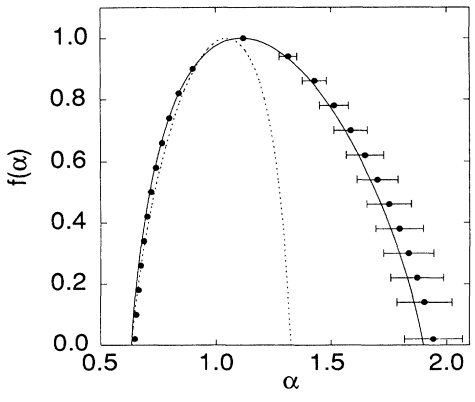

FIG. 22. $f(\alpha)$ curves for the experimental data (●), for theoretical data from a sine-circle map at criticality (——), and for a subcritical experimental data set (— — —) with $R/R_c = 12.375$ and $1/\mathrm{Pr} = 14.17$. The error bars for α that are smaller than 1.1 are of the order of the data points and are not plotted.

the universality of a particular map. For inflection points of the type $\theta|2\theta|^{\nu-1}$ we have that $\nu=2\ln s_1/\ln s_2=\alpha_{\max}/\alpha_{\min}$ [26]. From the experimental data for $\rho_g^{(4)}$, Fig. 13, we get $\nu=3.1\pm0.3$, putting the state in the universality class of the sine-circle map (1). Other golden-mean lines in our parameter space, $\rho_g^{(2)}$ and $\rho_g^{(3)}$, yield $\nu^{(2)}=2.9\pm0.3$ and $\nu^{(3)}=2.8\pm0.4$.

V. CONCLUSIONS

We have presented experimental data on the quasiperiodic regime of Rayleigh-Bénard convection in a ^{3}He–superfluid-^{4}He mixture. The quasiperiodic motions are two internal oscillatory modes of the system and are shown to lead to mode-locked and chaotic states. The parameter space of Rayleigh and Prandtl numbers is explored and mode-locked regions are identified. The critical line of the circle map model is located using transient Poincaré sections to study the stability eigenvalues of periodic points within resonance horns. This is a powerful technique that can be utilized effectively even in systems such as thermal convection that are intrinsically higher dimensional. We have also implemented a number of techniques for the analysis of nonlinear dynamical systems, particularly those thought to correspond to the universality class of a one-dimensional-map model. These techniques are robust both in the presence of noise and using small data sets, and should have wide applicability. In particular, our determination of the trajectory scaling function by fitting the experimental map is an example of techniques now being investigated for interpolating the behavior of dynamical systems as a function of the control parameter. Finally, we have demonstrated that for a number of points in the experimental parameter space the universal predictions of the sine-circle map are satisfied to remarkable precision. This constitutes a very severe test for the genericity and universality of the circle-map predictions, since systems with two internal frequencies cannot be manipulated to provide optimal conditions for circle-map behavior.

ACKNOWLEDGMENTS

We would like to acknowledge useful discussions with P. Cvitanović, M. Feigenbaum, I. Kevrekidis, and J. Lowenstein. This work was funded by the U.S. Department of Energy, Office of Basic Energy Science, Division of Materials Science.

APPENDIX: GENERAL EXPRESSIONS FOR THE SCALING FUNCTION

When the winding number is not the golden mean, the segments that go into the computation of the scaling function are no longer given by the Fibonacci numbers. In this appendix we will explain a few details of the order of the segments along the circle and how to compute the scaling function.

For an irrational winding number ρ there are a series of approximants P_n/Q_n that are determined from truncations of the continued fraction expansion of ρ. If

$$\rho=\langle a_1,a_2,a_3,\ldots\rangle\ , \tag{A1}$$

then

$$\frac{P_0}{Q_0}=\frac{0}{1},\frac{P_1}{Q_1}=\frac{1}{a_1},\frac{P_2}{Q_2}=\frac{1}{a_1+\dfrac{1}{a_2}} \tag{A2}$$

and in general one has the recursions

$$\begin{aligned}P_{n+1}&=a_{n+1}P_n+P_{n-1}\ ,\\ Q_{n+1}&=a_{n+1}Q_n+Q_{n=1}\ .\end{aligned} \tag{A3}$$

By definition the approximant P_0/Q_0 is the fraction 0/1. The nth approximant for a periodic continued fraction has the property that it approximates the irrational ρ by CQ_n^{-1}, for a constant C independent of n.

For each approximant to the irrational winding number, one has an orbit of Q_n points labeled x_0 through x_{Q_n-1}. This orbit is not a periodic orbit since x_{Q_n}, the next orbit point, is not the point x_0, but it is a close approximation to one. The error $x_0-x_{Q_n}$ goes asymptotically as α^n, with α the eigenvalue 1.2558... of the circle-map renormalization group.

The point closest to x_0 with respect to the coordinate is $x_{Q_{n-2}}$ and on the other side of x_0 along the circle is $x_{Q_{n-1}}$. In general, the segment between x_0 and $x_{Q_{n-1}}$ is the largest segment generated by the orbit with Q_n points. In analogy with the sine-circle map we choose

$$\Delta_0^{(n)}=[x_0,x_{Q_{n-1}}] \tag{A4}$$

and define the other segments as its iterates

$$\Delta_k^{(n)}=f^{(k)}(\Delta_0^{(n)})=[x_k,x_{Q_{n-1}+k}]\ , \tag{A5}$$

where the index calculations are done modulus Q_n.

For the purpose of computing the scaling function, one does not consider all Q_n segments, but just the iterations of $\Delta_0^{(n)}$ that do not share a common end point. These are the segments of label 0 through $Q_{n-2}-1$, and do not cover the whole circle.

The scaling function $\sigma(s)$ is formed by the concatenation of piecewise constant steps σ_t. The number of steps is one of the Fibonacci numbers in the sequence $\{F_0,F_1,F_2\ldots\}$ with $F_0=1$ and $F_1=2$. The steps σ_t that form the scaling function are the ratios between segments at different levels, the larger segment being the "parent segment" and the smaller segment being the "child segment." If the winding number is the golden mean, the parent and child segments can be expressed in terms of the Fibonacci numbers, but if the winding number is just the golden-mean tail, then one has to introduce a binary Fibonacci base to express them.

Any positive integer s can be written in the form

$$s=\epsilon_0F_0+\epsilon_1F_1+\epsilon_2F_2+\epsilon_3F_3+\cdots \tag{A6}$$

with any of the ϵ_i taking the values 0 or 1 and the F_i as defined above. The sequence of ϵ_i is a binary Fibonacci representation of the integer s, and is written from the most significant ϵ to the least significant ϵ as in

$(\epsilon_k, \epsilon_{k-1}, \ldots, \epsilon_0)$. It is not unique because some integers can be written in more than one way. For example, the integer 3 can be written as (0,1,1) or as (1,0,0). To make the binary Fibonacci expansion unique we introduce the convention that there cannot be two successive 1's in the binary expansion [53]. In the example, (1,0,0) would be the representation of 3.

We define the scaling function using two index functions: the child function $\theta_n(s)$ and the parent function $\Theta_n(s)$ to be defined later.

$$\sigma(s)=\lim_{n\to\infty}\frac{|\Delta_{\theta_n}(\lfloor sF_n\rfloor)|}{|\Delta_{\Theta_n}(\lfloor sF_n\rfloor)|}\ , \tag{A7}$$

where we used the floor function $\lfloor x\rfloor$, which returns the largest integer smaller than x. The child and parent functions depend on the approximants P_n/Q_n being used.

To compute the child function for an integer s one first decomposes s into its binary Fibonacci expansion $(\epsilon_k, \epsilon_{k-1}, \ldots \epsilon_1, \epsilon_0)$, chooses an offset $m \geq 0$, and evaluates the sum

$$\theta_n(s)=\epsilon_0 Q_{n-k-m}+\epsilon_1 Q_{n-k+1-m} + \cdots +\epsilon_{k-1}Q_{n-1-m}+\epsilon_k Q_{n-m}\ . \tag{A8}$$

In practice, to improve the convergence, one has to choose the offset m to be at least 1. The parent function is evaluated using the same offset m,

$$\Theta_n(s)=\epsilon_0 Q_{n-k-m} +\epsilon_1 Q_{n-k+1-m}+\cdots+\epsilon_{k-1}Q_{n-1-m}\ . \tag{A9}$$

The parent function differs from the child function only by the omission of the last term of the sum.

[1] K. Kaneko, *Collapse of Tori and Genesis of Chaos in Dissipative Systems* (World Scientific, Singapore, 1986).
[2] J. Glazier and A. Libchaber, IEEE Trans. Cir. Sys. **35**, 790 (1988).
[3] R. Ecke, in NATO Advanced Study Institute–Chaos, Orders, and Patterns, edited by P. Cvitanović and R. Artuso (Plenum, New York, in press).
[4] S. Shenker, Physica D **5**, 405 (1982).
[5] S. Ostlund, D. Rand, J. Sethna, and E. Siggia, Physica D **8**, 303 (1983).
[6] M. Feigenbaum, L. P. Kadanoff, and S. J. Shenker, Physica D **5**, 370 (1982).
[7] M. Jensen, P. Bak, and T. Bohr, Phys. Rev. A **30**, 1960 (1984).
[8] P. Cvitanović, M. Jensen, L. Kadanoff, and I. Procaccia, Phys. Rev. Lett. **55**, 343 (1985).
[9] M. Jensen, L. Kadanoff, A. Libchaber, I. Procaccia, and J. Stavans, Phys. Rev. Lett. **55**, 2798 (1985).
[10] A. Fein, M. Heutmaker, and J. Gollub, Phys. Scr. **T9**, 79 (1985).
[11] E. G. Gwinn and R. M. Westervelt, Phys. Rev. Lett. **57**, 1060 (1986).
[12] J. Maurer and A. Libchaber, J. Phys. (Paris) Lett. **40**, L419 (1979).
[13] M. Sano and Y. Sawada, in *Turbulence and Chaotic Phenomena in Fluids,* edited by T. Tatsumi (North-Holland, Amsterdam, 1983), pp. 167–172.
[14] J. Gollub and S. Benson, J. Fluid Mech. **100**, 449 (1980).
[15] H. Haucke and R. Ecke, Physica D **25**, 307 (1987).
[16] R. Mainieri, T. Sullivan, and R. Ecke, Phys. Rev. Lett. **63**, 2357 (1989).
[17] J. Peinke, J. Parisi, R. Huebner, M. Duong-van, and P. Keller, Europhys. Lett. **12**, 13 (1990).
[18] M. Bauer, U. Krueger, and W. Martienssen, Europhys. Lett. **9**, 191 (1989).
[19] T. Bohr, P. Bak, and M. Jensen, Phys. Rev. A **30**, 1970 (1984).
[20] T. Bohr, Phys. Rev. Lett. **54**, 1737 (1985).
[21] X. Wang, R. Mainieri, and J. Lowenstein, Phys. Rev. A **40**, 5382 (1989).
[22] D. Sullivan, in *Non-linear Evolution and Chaotic Phenomena,* edited by P. Zweifel, G. Gallavotti, and M. Anile (Plenum, New York, 1987), pp. 101–110.
[23] M. J. Feigenbaum, Nonlinearity **1**, 577 (1988).
[24] R. Mainieri and R. Ecke (unpublished).
[25] T. Halsey, M. Jensen, L. Kadanoff, I. Procaccia, and B. Shraiman, Phys. Rev. A **33**, 1141 (1986).
[26] M. J. Feigenbaum, J. Stat. Mech. **46**, 925 (1987).
[27] Vespel is a graphite-loaded polyimide resin produced by Dupont, Wilmington, DE 19898.
[28] Y. Maeno, H. Haucke, R. Ecke, and J. Wheatley, J. Low-Temp. Phys. **59**, 305 (1985).
[29] G. Metcalf and R. Behringer, Phys. Rev. A **41**, 5735 (1990).
[30] N. Packard, J. Crutchfield, J. Farmer, and R. Shaw, Phys. Rev. Lett. **45**, 712 (1980).
[31] F. Takens, in Lecture Notes in Mathematics Vol. 898, edited by D. A. Rand and L-S. Young (Springer, Berlin, 1981), pp. 366–381.
[32] J. -P. Eckmann and D. Ruelle, Rev. Mod. Phys. **57**, 617 (1985).
[33] A. Fraser and H. Swinney, Phys. Rev. A **33**, 1134 (1986).
[34] R. Ecke and I. Kevrekidis, Phys. Lett. A **131**, 344 (1988).
[35] R. Ecke and H. Haucke, J. Stat. Phys. **54**, 1153 (1989).
[36] R. Ecke, Y. Maeno, H. Haucke, and J. Wheatley, Phys. Rev. Lett. **53**, 1567 (1984).
[37] R. Ecke, H. Haucke, Y. Maeno, and J. Wheatley, Phys. Rev. A **33**, 1870 (1986).
[38] R. Deissler, R. Ecke, and H. Haucke, Phys. Rev. A **36**, 4390 (1987).
[39] D. Rand, in *Proceedings of the Eighth International Congress of Mathematical Physics,* edited by M. Mebkhout and R. Seneor (World Scientific, Singapore, 1987).
[40] D. Aronson, M. Ghory, G. Hall, and R. McGehee, Commun. Math. Phys. **83**, 303 (1982).
[41] J. A. Glazier, G. Gunaratne, and A. Libchaber, Phys. Rev. A **37**, 523 (1988).
[42] J. Stavans, S. Thomae, and A. Libchaber, in *Dimensions and Entropies in Chaotic Systems,* edited by G. Mayer-Kress, Springer Series in Synergetics Vol. 32 (Springer-Verlag, Berlin, 1986), pp. 207–214.
[43] M. J. Feigenbaum, Commun. Math. Phys. **77**, 65 (1980).
[44] Y. Sinai, Russ. Math. Surveys **166**, 21 (1972).
[45] R. Bowen, Trans. Am. Math. Soc. **154**, 377 (1971).
[46] D. Ruelle, Trans. Am. Math. Soc. **185**, 237 (1973).
[47] T. C. Halsey *et al.*, Phys. Rev. A **33**, 1141 (1986).

[48] P. Grassberger, Phys. Lett. A **97**, 227 (1983).
[49] M. J. Feigenbaum, J. Stat. Phys. **46**, 919 (1987).
[50] A. Chhabra and R. V. Jensen, Phys. Rev. Lett. **62**, 1327 (1989).
[51] A. B. Chhabra, R. V. Jensen, and K. R. Sreenivasan, Phys. Rev. A **40**, 4593 (1989).
[52] A. Arneodo and M. Holschneider, Phys. Rev. Lett. **58**, 2007 (1987).
[53] D. E. Knuth, *The Art of Computer Programming, Vol. 1. Fundamental algorithms*, 2nd ed. (Addison-Wesley, Reading, MA, 1973), see exercise 1.2.8.34.